Journal of Power Sources 271 (2014) 82–86

Contents lists available at ScienceDirect

Journal of Power Sources

journal homepage: www.elsevier.com/locate/jpowsour

Short communication

Real-time displacement and strain mappings of lithium-ion batteries using three-dimensional digital image correlation

P.K. Leung [a, *], C. Moreno [a], I. Masters [a, *], S. Hazra [a], B. Conde [b], M.R. Mohamed [c], R.J. Dashwood [a], R. Bhagat [a]

[a] WMG, University of Warwick, Gibbet Hill Road, Coventry CV4 7AL, UK
[b] School of Engineering, University of Warwick, Gibbet Hill Road, Coventry CV4 7AL, UK
[c] Faculty of Electrical & Electronics, Universiti Malaysia Pahang, Pekan, Pahang 26600, Malaysia

HIGHLIGHTS

- First application of 3D-DIC for battery displacement and strain analyses.
- Quantified displacement and strain data in the *x*-, *y*- and *z*-directions.
- Identified relationships between displacements, surface strains and cell structure.

ARTICLE INFO

Article history:
Received 17 March 2014
Received in revised form
21 July 2014
Accepted 30 July 2014
Available online 7 August 2014

Keywords:
Digital image correlation
Lithium-ion battery
Principal strain
stress
von-Mises strain

ABSTRACT

This work presents the first application of three-dimensional digital image correlation for real-time displacement and strain analysis of a pouch type lithium-ion battery. During the electrochemical charge–discharge processes, displacements in the *x*-, *y*- and *z*-directions vary at different states-of-charge (SOCs) attributed to the expansion and the contraction of the interior structure. The *z*-displacement is observed to develop and concentrate at the vicinity of the openings of the jelly-roll structure. By resolving the displacement components, the progression and distribution of the surface strains, including principal and von-Mises strains, are computed in the charge–discharge processes. It is shown that the dominant strains are up to 0.12% in the rolling direction of the jelly-roll structure and distribute uniformly on the *x*–*y* plane over the surface.

1. Introduction

Lithium-ion batteries (LIBs) have been the most widely used energy storage device for portable electronics. Due to their high specific energy, long cycle life and slow self-discharge, LIBs are considered to be suitable for electric and hybrid vehicle applications. For automobile industry, electrochemistry and mechanical integrity are important aspects to design the lithium-ion batteries from cell to module levels [1,2]. Similar to most electrochemical energy storage systems, the chemical compositions of the active materials change during the charge–discharge processes. This induces strains in electrode particles and causes changes in electrode volume. The induced strain is considered to be the main cause of material cracking and other forms of performance degradation [3]. To evaluate the mechanism of strain generation during the electrochemical intercalation and de-intercalation processes, a number of theoretical and computational models have been developed at particle and electrode levels [4–6].

In comparison, the evolutions of stresses and strain in battery components have been investigated experimentally by only a few researchers using linear voltage displacement transducer (LVDT) [1], wafer curvature method [3] and two-dimensional digital image correlations (2D DIC) [7,8]. The reported methods were still limited to the electrode level and are completely based on two-dimensional measurements. In the cases of both LVDT and wafer curvature methods, strain measurements can only be made locally at the points where the devices are mounted or bonded appropriately on the specimen surface. DIC is a non-contact optical

* Corresponding authors.
E-mail addresses: P.leung@warwick.ac.uk, p.leung@uma.es (P.K. Leung), I.Masters@warwick.ac.uk (I. Masters).

http://dx.doi.org/10.1016/j.jpowsour.2014.07.184
0378-7753/

technique that has been found increasing numbers of applications in different areas of engineering. This technique enables strain to be measured directly by tracking a unique pattern on the surface through a sequence of digital images.

In conventional DIC technique, strain data is limited in two dimensions (*x*- and *y*-directions) as a single sensor is used to capture the digital images. To allow three-dimensional measurements (*x*-, *y*- and *z*-directions), a plurality of synchronized stereo sensors are required and combined with the photogrammetric theories. The three-dimensional measurement provides a more complete description of the volume change to the battery in the typical electrochemical operations.

To the best knowledge of the authors, this work is the first to propose the use of three-dimensional DIC (3D DIC) for real-time displacement and strain measurements for energy storage applications. In this paper, qualitative displacement and strain data were provided as a function of state-of-charge (SOC) in the *x*-, *y*- and *z*-directions. With this information, the principal and von-Mises strain values were computed and observed to increase gradually in the charging process.

2. Experimental procedures

The battery investigated was a pouch type lithium-ion polymer battery supplied by Lishen Battery Co. (model PP053759, China). The battery is based on nickel–manganese–cobalt oxide (NMC) chemistry and has a nominal capacity of *c.a.* 1200 mA h. Inside the aluminium-plastic pouch, the interior structure illustrated in Fig. 1a is constructed by winding the ribbon-like electrode and separator to form a 'jelly-roll' structure. The negative and positive active materials of *c.a.* 80 and 60 μm are coated on each side of the separator materials (*c.a.* 25 μm). Thin layers of copper and aluminium foils (*c.a.* 10 μm) are used as the current collectors.

During the three-dimensional strain measurement, a galvanostatic charge–discharge cycle was carried out at constant current (1200 mA, 1-C rate) at 22.5 °C using a Bio-logic VMP3 potentiostat. To eliminate the strain attributed to the gas build-up, the measurements were made directly on the interior structure. As shown in Fig. 1b, the battery was charged up to a cell voltage of 4.1 V followed by a taper charge of this potential (4.1 V) for an overall charge cycle of 1 h. After that, the discharge is performed using the same current down to a cut-off voltage of 2.8 V. The state-of-charge

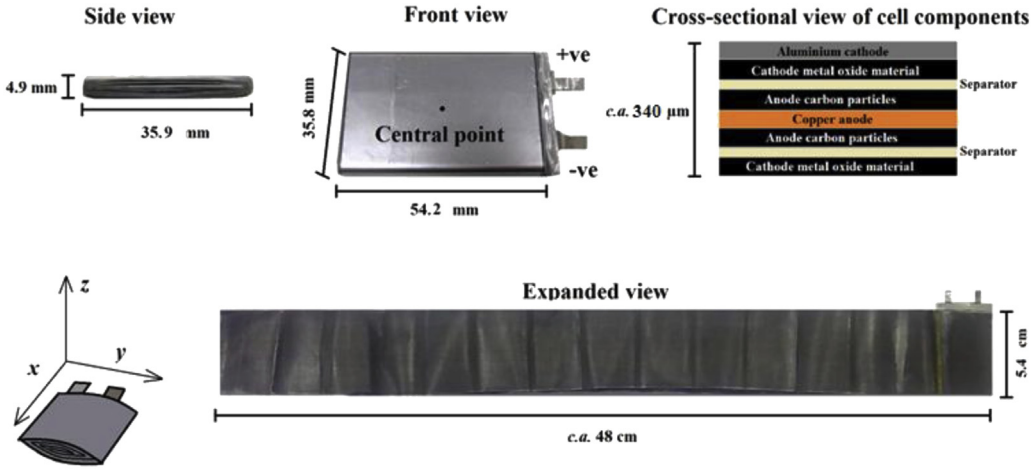

(a)

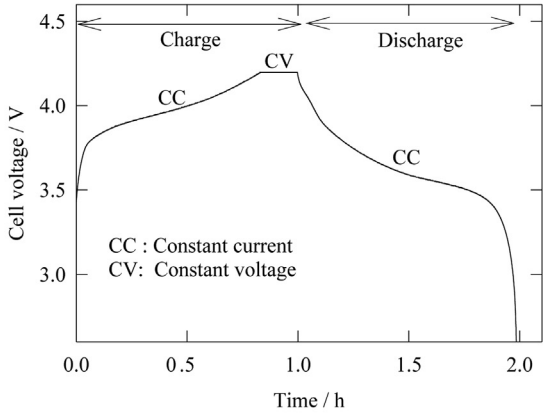

(b)

Fig. 1. Schematics of the pouch type lithium-ion battery: (a) internal jelly-roll structure, (b) charge–discharge voltage profile at 1-C rate.

(SOC) of the battery was defined as the percentage of the charged capacity over its rated value (*c.a.* 1200 mA h).

The 3D DIC analysis was conducted by using the GOM Aramis system (Germany) comprising a pair of stereo sensors and a data-processing software. The two sensors had a resolution of up to 1.3 megapixels and were equipped with 50 mm lenses. The two digital sensors were mounted at *c.a.*800 mm above the battery specimen. Before the experiment, the system was calibrated using the calibration panel at the orientations as requested following the manufacturer's recommended procedure. To ensure the measurement volume and the sensor positions were aligned properly, the calibration deviation were maintained within 0.02 pixels [9]. In a typical test, the DIC system requires the surface of the battery specimen to be sprayed with a random speckle pattern, which was tracked during the test. After adjusting the light source and the shutter speed, images were recorded at a regular time interval of 15 s over 140 min (560 images).

During the analysis of the digital images, the areas at the edges were eliminated from the analysing area. This is because the facets at the edges tend to be matched with the incorrect facets. The selected analysing area was therefore limited to 29 mm × 49 cm. After defining the starting point, the surface points were computed within the digital image at the reference stage. These data point were then tracked at sub-pixel accuracy to measure the displacement over the specimen surface by means of square facets in the *x*-, *y*- and *z*-directions. The facet size used in this study was 15 × 15 pixels. Subsequent data processing, such as principle strain vectoring and von-Mises strain calculation, were performed in the ARAMIS® software.

3. Results and discussions

During the 3D DIC measurement, the selected LIB underwent a galvanostatic charge–discharge cycle at 1C-rate (1200 mA). As shown in Fig. 2a, the displacement in *z*-direction (at the centre of the battery) increased steadily and reached 177 μm at the fully charged state, and then decreased down to 55 μm after the discharge process. The resulting strain value in *z*-direction was up to 3.67% (177 μm ÷ 4.9 mm thickness), which is in agreement with the previous work (1.5%) reported at 0.4C charge–discharge rate. The variation of the *z*-displacement depended upon the thickness increment of the 'jelly-roll' structure. In the charge–discharge processes, the reversible trend of the *z*-displacement is attributed to the lattice expansion and contraction process of the active materials. In the charging process, the overall expansion is mainly caused by the negative lithiated carbon electrode, while the positive NMC electrode actually undergoes contraction. This is because the volume expansion of lithiated carbon (*c.a.* 7–12% [10,11]) is far more significant than the volume contraction of the NMC oxides (*c.a.* 1% [12,13]). It also needs to take account that the negative electrode volume often occupies more than 30% of the overall 'jellyroll' volume [13] (up to 45% in this work).

However, the lattice expansion and contraction of the active materials has been reported to be a highly reversible process (up to *c.a.* 100% reversibility for the lithiated carbon [10]). This means that,

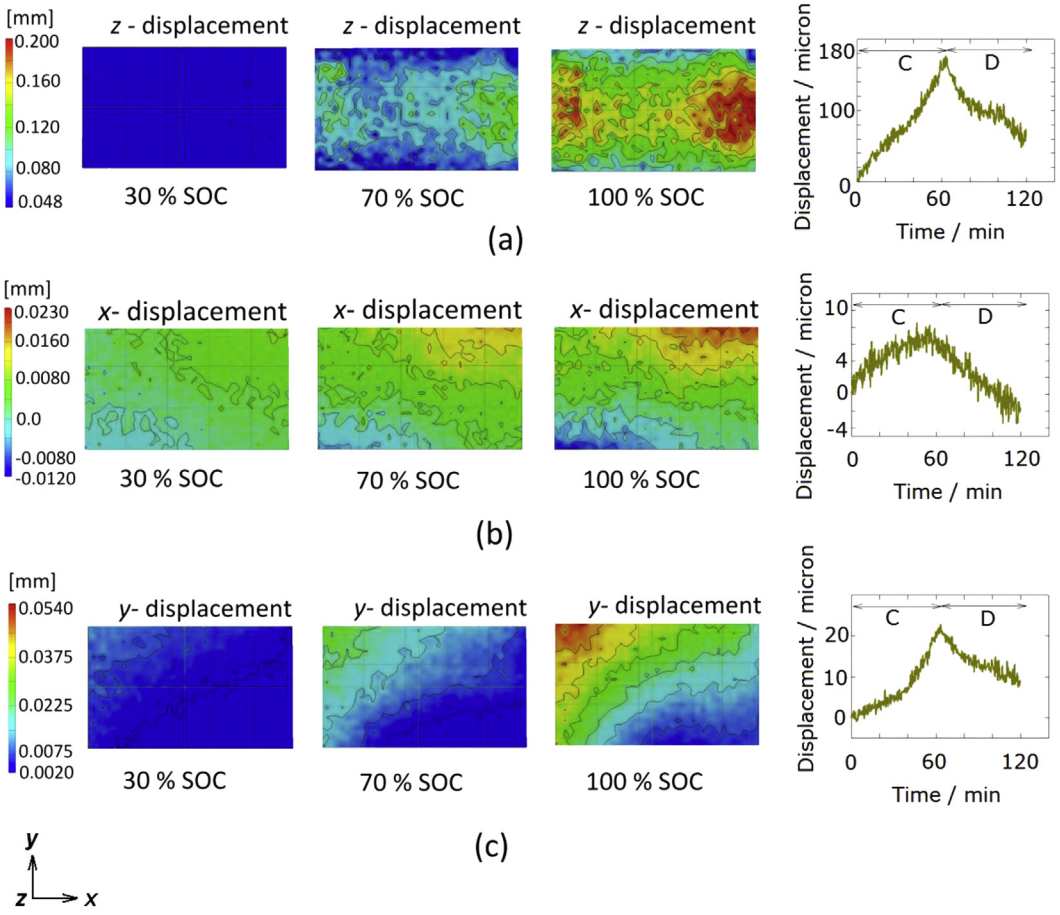

Fig. 2. Displacement distributions of the lithium-ion battery at 30%, 70% and 100% SOC: (a) *z*-displacement, (b) *x*-displacement and (c) *y*-displacement. Displacement *vs.* time curves are based on the central point of the battery.

after expansion in the charging process, the active materials can contract back to its original size at the end of the discharge cycle. In contrast, physical and electrochemical swellings caused by binder expansion and particle stacking are less reversible [3,10]. This explains the phenomenon that the residual *z*-displacement was observed after the charge–discharge cycle.

The progression and distribution of *z*-displacement at different SOCs are illustrated in Fig. 2a. In the initial state, the contour pattern was relatively uniform over the surface. While charging the battery, the displacement in *z*-direction developed and concentrated on the left and right sides of the battery. These regions are at the vicinity of the openings of the 'jelly-roll' structure (Please refer to Fig. 1a), which are less constrained to enable displacement and relaxation to take place than the other parts of the structure. When the battery was fully charged, the *z*-displacements in these regions were observed to reach *c.a.*200–220 μm. These values were approximately 30–40 μm higher than those in the central areas (*c.a.*160–180 μm).

Compared to the increment of *z*-displacement, the displacement values in *x*- and *y*-directions were relatively small (<60 μm). This is consistent with the description of Oh et al. [13] with the use of LVDT method. When the battery is under charge, each sandwich electrode layer tends to curve in the *z*-direction within the 'jelly-roll' structure. This feature has been further modified and employed as the 'wafer curvature method' for the strain measurement studies of LIB electrodes [3]. Despite the dominance of the *z*-displacement, the resulting *x*- and *y*-displacement distributions were determined by the DIC system as illustrated in Fig. 2b and c. Fig. 2b shows that the displacement in *x*-direction progressed mainly on the upper-right side and decreased slightly on the lower-left side during the charging process. On the contrary, the displacements in the *y*-direction (Fig. 2c) tended to be larger and smaller on the upper-left and the lower-right sides of the battery, respectively.

As in the case of the *z*-displacement, the *x*- and *y*-displacements in the central area increased and decreased in the charge–discharge processes. As shown in Fig. 2b and c, the *x*- and *y*-displacements increased up to *c.a.* 5.0 μm and *c.a.*22.5 μm at the fully charged state, and decreased down to *c.a.* −2.2 μm and *c.a.* 10.5 μm as the residual displacements after the discharge process.

After obtaining the displacement components, principle strains and their corresponding directions were computed on the *x*–*y* plane using Equations (1) and (2):

$$\varepsilon_{1,2} = \frac{\varepsilon_{xx}+\varepsilon_{yy}}{2} \pm \sqrt{\left(\frac{\varepsilon_{xx}-\varepsilon_{yy}}{2}\right)^2 + \left(\frac{\gamma_{xy}}{2}\right)^2} \quad (1)$$

$$\Theta = \frac{1}{2}\tan_{-1}\left(\frac{2\gamma_{xy}}{\varepsilon_x - \varepsilon_y}\right) \quad (2)$$

where $\varepsilon_{1,2}$ are the major and minor principal strains; Θ is the principal angle; ε_{xx} and ε_{yy} are the strains acting on the planes normal to the *x*- and *y*-axes, respectively; γ_{xy} is the shear strain acting on the plane normal to the *x*-axis directed to the *y*-direction. These equations were based on 'plane strain state', which are two-dimensional simplifications used for thick structures. It should be noted that 'surface strain' only takes account of the in-plane strains in most mechanical calculations. In this study, the 'in-plane' surface strains are in the *x*- and *y*-directions (Please see Fig. 1). Therefore, the strains in *z*-direction are out of plane and exhibit through the thickness of the battery.

Fig. 3a shows the evolutions of the major principal strains on the *x*–*y* plane during the charging process. The black and white arrows represent the directions of the major and minor principal strains, respectively. Most of the major principal strains aligned in the *y*-direction and developed uniformly over the surface. On the contrary, minor strain tends to be smaller (−0.06 to +0.03%) and orient in the *x*-direction. Compared to the *z*-displacement, the surface strain distributions were more uniform as they only correspond to the top surface of the battery, while the *z*-displacement takes account of the thickness of the whole battery structure (out-of-plane).

The major strain direction observed (*y*-direction) is associated with the design of the 'jelly-roll' structure. This is similar to the case of a pressurized cylinder, in which the corresponding 'hoop strain' is developed in the tangential direction to resist the inflation effect caused by the internal pressure. This shows that the major strains on the *x*–*y* plane were generated uniformly in the rolling direction (*y*-direction) and attributed to the expansion of the 'jelly-roll' structure.

To evaluate the overall 'surface strains' on the *x*–*y* plane, the multiple principal and shear strain components were resolved into a single strain value regardless of the direction using the von-Mises strain equation:

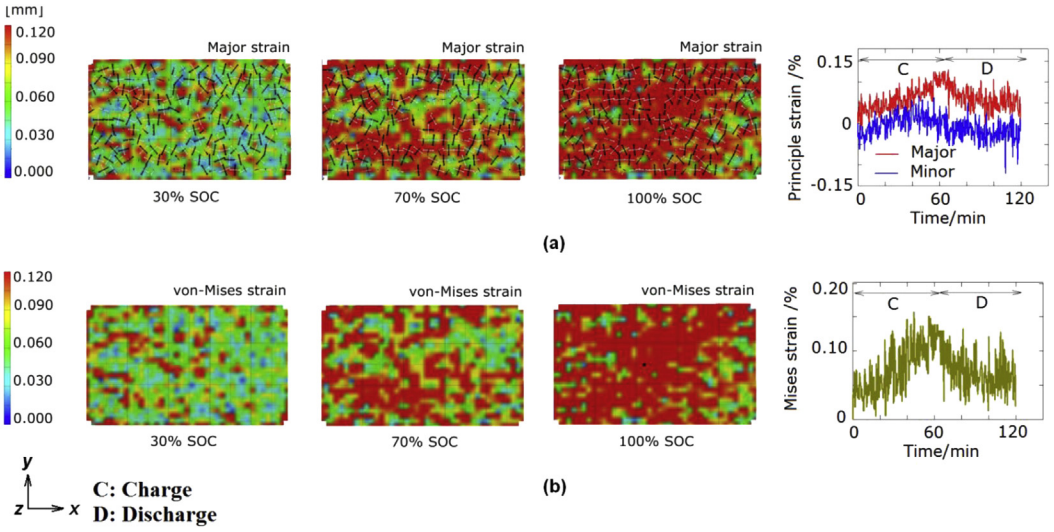

Fig. 3. Strain distribution of the lithium-ion battery at 30%, 70% and 100% SOC: (a) major strains, (b) von-Mises strains. Strain *vs.* time curves based on the central point of the battery. (Black arrow: Major strain directions; white arrow: Minor strain directions).

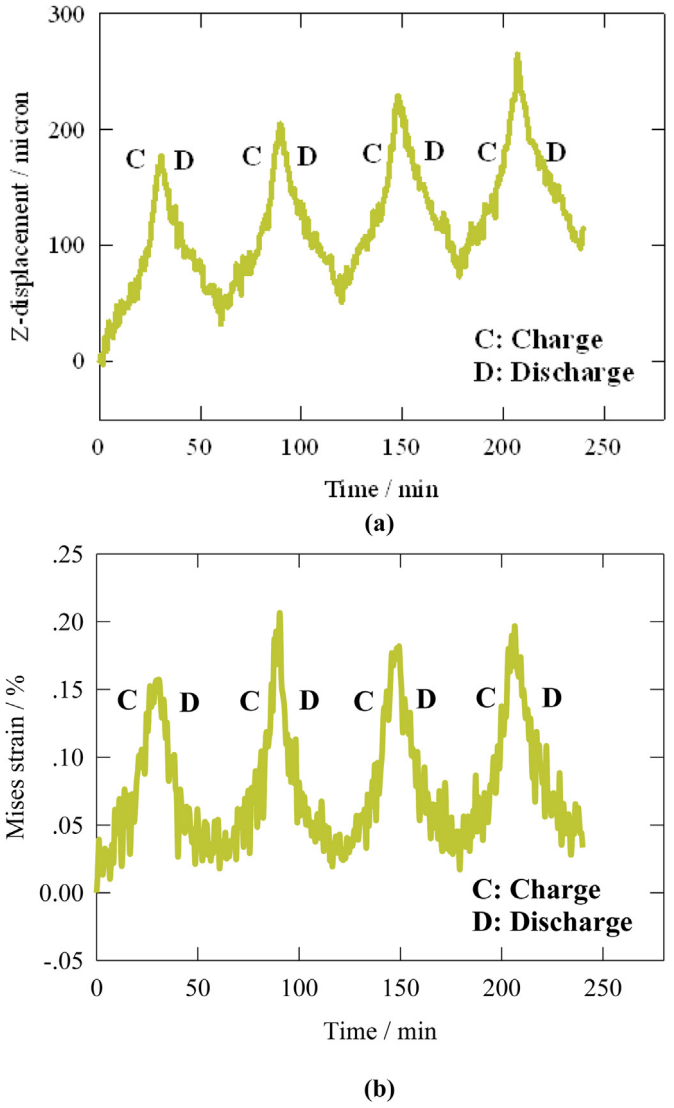

Fig. 4. Evolutions of (a) *z*-displacement and (b) von-Mises strain of the lithium-ion battery under 4 continuous charge–discharge cycles at 1-C rate. Measurements are based on the central point of the battery.

$$\varepsilon_{v.m} = \sqrt{\frac{2}{3}(\varepsilon_1^2 + \varepsilon_2^2)} \quad (3)$$

where $\varepsilon_{v.m}$ is the von-Mises strain; ε_1 and ε_2 are the major and minor principal strains. Fig. 3c shows the progression and distribution of the von-Mises strains on the *x*–*y* plane at different SOCs. The von-Mises strain values were observed to increase at a gradual rate in the charging process. When the battery was at 100% SOC, the von-Mises strains reached up to *c.a.* 0.15% and distributed uniformly over the surface. It is also shown that the magnitude and the distribution of the von-Mises strain were similar to those of the major strains in the *y*-direction. This is because the principal strains in the *y*-direction were significantly higher than in the *x*-direction. This further justifies that the strains in the *y*-direction (rolling direction of the 'jelly-roll' structure) were the most dominants strains generated on the battery surface.

Using these explanations, the developments of *z*-displacement and von-Mises strain were also evaluated under continuous charge–discharge cycling. As shown in Fig. 4a, the *z*-displacement increased gradually after each cycle. At the end of the 4th cycle, the *z*-displacement was about 100 μm from its original value (0 μm). Compared to the *z*-displacement data, Fig. 4b shows the increment of von-Mises strain was less significant (0.05%). This is because the displacement or strain in *z*-direction is out of plane and exhibit through the thickness of the whole battery structure, while von-Mises strain is mainly attributed to the surface strains in the *x*–*y* plane.

4. Conclusions

In conclusion, the three-dimensional digital image correlation is shown to be an efficient and accurate technique to measure the displacement and strain distributions of the pouch type lithium-ion batteries. During the electrochemical charge–discharge processes, the displacements in the *x*-, *y*- and *z*-directions vary at different states-of-charge (SOCs) attributed to the expansion and the contraction of the interior structure. The *z*-displacement is observed to develop and concentrate at the vicinity of the openings of the jelly-roll structure. By resolving the displacement components, the computed surface strains, including principal and von-Mises strains, were shown to increase and decrease in the charge and discharge processes, respectively. The most dominant strains were observed in the rolling direction of the 'jelly-roll' structure and distributed uniformly on the *x*–*y* plane over the surface.

References

[1] R. Fu, M. Xiao, S.-Y. Choe, J. Power Sources (2013) 211–244.
[2] E. Sahraei, R. Hill, T. Wierzbicki, J. Power Sources (2012) 307–321.
[3] V.A. Sethuraman, N. Van Winkle, D.P. Abraham, A.F. Bower, P.R. Guduru, J. Power Sources (2012) 334–342.
[4] X. Zhang, W. Shyy, A. Sastry, J. Electrochem. Soc. 154 (2007) A910–A916.
[5] X. Zhang, A. Sastry, W. Shyy, J. Electrochem. Soc. 153 (2006) A1019–A1030.
[6] R.E. Garcia, Y. Chiang, W.C. Carter, P. Limthongkul, C.M. Bishop, J. Electrochem. Soc. 152 (2005) A255–A263.
[7] J. Chen, J. Liu, Y. Qi, T. Sun, X. Li, J. Electrochem. Soc. (2013) A1502–A1509.
[8] Y. Qi, S.J. Harris, J. Electrochem. Soc. (2010) A741–A747.
[9] T.L. Jin, N.S. Ha, N.S. Goo, Thin Wall. Struct. (2014), http://dx.doi.org/10.1016/j.tws.2013.10.012.
[10] N. Zhang, H. Tang, J. Power Sources (2012) 52–55.
[11] T. Ohzuku, Y. Iwakoshi, K. Sawai, J. Electrochem. Soc. (1993) 2490–2498.
[12] Y. Koyama, I. Tanaka, H. Adachi, Y. Makimura, T. Ohzuku, J. Power Sources (2003) 644–648.
[13] K.-Y. Oh, J.B. Siegel, L. Secondo, S.U. Kim, N.A. Samad, J. Qin, D. Anderson, K. Garikipati, A. Knobloch, B.I. Epreanu, C.W. Monroe, A. Stefanopoulou, J. Power Sources (2014) 197–202.